Environmental Science Nano

Emerging investigator series: Quantifying silver nanoparticle aggregation kinetics in real-time using particle impact voltammetry coupled with UV-vis spectroscopy

Journal:	*Environmental Science: Nano*
Manuscript ID	EN-ART-05-2020-000490.R2
Article Type:	Paper

Emerging investigator series: Quantifying silver nanoparticle aggregation kinetics in real-time using particle impact voltammetry coupled with UV-vis spectroscopy

Laela Ezra[a,†], Zachary J. O'Dell[a,†], Janan Hui[a], and Kathryn R. Riley[a,*]

[a]*Department of Chemistry and Biochemistry, Swarthmore College, Swarthmore, PA 19081, USA*

[†]L. Ezra and Z.J. O'Dell contributed equally to this work.

*Corresponding author: Tel: +1-610-690-3904, email: kriley1@swarthmore.edu

Abstract: The aggregation of silver nanoparticles (AgNPs) as they encounter biological and environmental systems can dictate their fate and transport. Here, we present a rapid, affordable, and robust analytical method for quantifying AgNP aggregation that combines a single particle electrochemistry technique called particle impact voltammetry (PIV) with the strengths of UV-vis spectroscopy. This orthogonal technique, designated PIV/UV-vis, enables the quantitative evaluation of aggregation kinetics by simultaneously measuring changes in the redox behavior of individual AgNPs and spectroscopic changes in the bulk AgNP colloidal solution. We demonstrate that the frequency of AgNP collisions measured by PIV is correlated to the concentration of monodisperse AgNPs in solution. In this way, aggregation can be quantified by the disappearance of AgNP collisions, much like in UV-vis where aggregation is quantified by the rate of disappearance of the localized surface plasmon resonance band of monodisperse AgNPs. The PIV/UV-vis technique was validated by determining the critical coagulation concentration (CCC) of 40 nm AgNPs in the presence of monovalent and divalent cations. The CCC values determined by PIV and UV-vis were in excellent agreement with one another and were determined as 43 ± 4 and 43 ± 3 mM Na^+ and 3.0 ± 0.3 and 3.0 ± 0.1 mM Mg^{2+}, respectively. Using dynamic light scattering, aggregation was confirmed by monitoring changes in AgNP hydrodynamic diameter and results show a clear distinction in aggregation behavior above the CCC. Further, zeta potential measurements were used to monitor changes in AgNP surface charge as another measure of colloidal stability. Overall, PIV/UV-vis is a powerful technique to measure AgNP aggregation due to its speed, affordability, reproducibility, and potential broad applicability.

Environmental Significance Statement: Engineered nanomaterials (ENMs) can undergo several physical transformations (e.g., dissolution, aggregation, formation of bio- and eco-coronas) as they encounter biological and environmental matrices. The ability to quantify these transformations is important to understanding the fate and transport of ENMs. The evolution of fast, cost-effective, sensitive, and reliable analytical methods affords more rapid advancement toward this end. This work describes the development and application of a novel analytical technique that integrates single nanoparticle electrochemistry with UV-vis spectroscopy to quantify silver nanoparticle (AgNP) aggregation in real-time. This orthogonal method has several advantages including short analysis times, low operating cost, ease of analysis, robust and reproducible quantification of AgNP aggregation behaviors, and potential future application to other metal and metal oxide ENMs.

INTRODUCTION

As of 2014, the development of "nano-enabled" products, those which contain engineered nanomaterials (ENMs), represented greater than a USD 1 trillion industry and was projected to reach USD 4.4 trillion by 2018.[1] Silver nanoparticles (AgNPs), which constitute approximately 25% of this market, are produced at a rate of about 500 tons per year and lead the global increase in production of nano-enabled consumer products.[2,3] A recent report estimates that the use of AgNPs alone will reach USD 2.45 billion by 2022.[4] AgNPs are a material of great interest due to their strong antibacterial and antimicrobial properties.[5] They are incorporated in products such as wound dressings and cosmetics in order to prevent infection,[6–9] but also in some textiles and fabrics, specifically athletic clothing, in order to prevent the growth of bacteria with unpleasant odors.[10–12] However, these desired properties can be altered as the AgNPs undergo physical transformations like dissolution, aggregation, and the formation of bio- and eco-coronas, encouraging discussion about the toxicity of AgNPs.[7,13–15] For example, the aggregation of AgNPs can influence their fate and transport in environmental systems.[16–18] Thus, understanding the physical transformations of AgNPs is pivotal to continued evaluation of their long-term effects on the environment. As a result, affordable, reliable analytical methods are needed to quantify AgNP transformations in relevant media.

AgNP aggregation is well-studied in the literature and is known to depend on a variety of factors, including AgNP coating and surface charge, as well as solution conditions such as pH, ionic composition, and ionic strength.[19–23] At large enough sizes, aggregates can sediment out of solution, which can have a significant impact on their transport. Thus, AgNPs are often electrostatically stabilized with charged molecules like citrate that form a repulsive barrier between neighboring particles and enable the formation of a stable, monodisperse colloidal

suspension. However, by increasing the ionic strength of the solution the electric double layer is compressed, the repulsive barrier is reduced, and the nanoparticles begin to aggregate. Derajaguin-Landau-Verwey-Overbeak (DLVO) theory is often used to model aggregation and can be used to determine the critical coagulation concentration (CCC), which is a useful quantitative parameter to assess the stability of ENMs in the presence of different electrolytes. The CCC is the electrolyte concentration at which the aggregation behavior transitions from the reaction-limited colloidal aggregation (RLCA) regime to the diffusion-limited colloidal aggregation (DLCA) regime.[24]

Many studies use dynamic light scattering (DLS) to measure AgNP aggregation by monitoring the increase in the hydrodynamic diameter of the particle with increasing electrolyte concentration.[20,25–30] Some studies have also employed UV-vis spectroscopy to quantify aggregation rates by monitoring changes in the localized surface plasmon resonance (LSPR) band of AgNPs.[27,31–34] Still, more robust, rapid, and affordable analytical techniques are needed. An emerging technique for the characterization of nanoscale materials is particle impact voltammetry (PIV).[35–39] PIV involves the detection of single nanoparticle redox events, which can be correlated to the concentration and diameter of ENMs in solution. PIV can be carried out in several modes, which has enabled its application to a wide range of ENMs, including Ag, Au, Pt, IrO_x, and ZnO[40–44], and even for the detection of single biomolecules.[45–47] Although PIV has significant potential for the characterization of nanoscale materials, it has yet to see widespread use for the assessment of ENM transformations, fate, and transport.

There have been two previous reports demonstrating the quantitative application of PIV to study AgNP aggregation.[48,49] In one study, AgNPs of varying diameter (14, 29, and 45 nm) were evaluated in solutions containing 90 mM KCl. Careful deconvolution of PIV particle size

distributions allowed the formation of particle clusters containing 1, 4, or 8 particles to be quantified as a function of time.[48] This work was later validated and the mathematical models expanded in a similar study of 10 nm AgNPs.[49] One drawback of the previously reported PIV analysis methods is that AgNP aggregation can only be monitored up to a certain aggregate size (estimated to be ≈150 nm).[48,50] Further, these prior studies were conducted with a single electrolyte (KCl) and electrolyte concentration (90 mM). Thus, the relationship between the PIV signal and the aggregation behavior of AgNPs in different regimes (RLCA vs. DLCA) and in the presence of different cations (*e.g.*, Na^+, Mg^{2+}) have not yet been defined.

Herein, we demonstrate the optimization of PIV and its coupling to UV-vis spectroscopy in a technique that we call PIV/UV-vis. The integration of these orthogonal techniques enables the behavior of individual AgNPs to be monitored (PIV) at the same time as the behavior of the bulk colloidal solution (UV-vis). The motivation for developing PIV/UV-vis was two-fold. First, we aimed to create a simple quantitative model for determining CCC values using PIV, which relies on peak counting instead of more complicated deconvolution of particle size distributions. The more established UV-vis aggregation experiments served as an integrated control for developing these mathematical models. Second, we believed PIV/UV-vis could provide reliable, quantitative aggregation data in a short analysis time (300 s) and for a modest cost (less than USD 20,000), thereby providing the nanotechnology community with a new analysis technique. Herein, we enumerate the theory of PIV in greater detail to provide background to the broader nanotechnology community, as well as demonstrate the development, optimization, and successful application of PIV/UV-vis to determine CCC values for AgNPs in the presence of monovalent and divalent cations. AgNP solutions were also characterized using auxiliary analyses including scanning electron microscopy (SEM), DLS, and zeta potential measurements.

EXPERIMENTAL

Chemicals and reagents

Sodium hydroxide pellets were purchased from Fisher Scientific (Waltham, MA). Sodium citrate monobasic (≥99.5%), sodium chloride (≥99.5%), magnesium chloride (≥99%), and nitric acid solution (70%) were purchased from Sigma Aldrich (St. Louis, MO). Citrate-stabilized NanoXact AgNPs (20 mg L^{-1} in 2 mM citrate) with a nominal diameter of 10, 20, 40, and 80 nm and citrate-stabilized BioPure AgNPs (1000 mg L^{-1} in 2 mM citrate) with a nominal diameter of 40 nm were purchased from nanoComposix (San Diego, CA) and used as-received.

A buffer solution containing 10 mM sodium citrate was prepared in Millipore water (18.2 MΩ.cm at 25°C) and the pH was adjusted to 5.0 through drop-wise addition of 1M and 0.1M NaOH. A 2.5 M stock solution of NaCl and 250 mM stock solution of $MgCl_2$ were prepared in Millipore water.

Nanoparticle Characterization

SEM measurements were conducted using a JEOL 7500F field-emission SEM (JEOL USA Inc.). NanoXact AgNP samples were directly pipetted onto silicon wafers and dried overnight. BioPure AgNP samples were diluted in Millipore water to a concentration of 20 mg L^{-1} and the dilute AgNP suspension was directly pipetted onto a silicon wafer and dried overnight. An accelerating voltage of 20.0 kV and a probe current of 5 μA were used for analysis. Image processing was performed using ImageJ (National Institutes of Health). All AgNPs were spherical. The size distributions of NanoXact AgNPs are reported in ESI Table S1 and represent the average and standard deviation of at least 100 particles. The size distribution of BioPure AgNPs was determined to be 41 ± 6 nm (n = 400).

A Malvern Zetasizer Nano ZS DLS instrument (Malvern Panalytical, Ltd.) was used to

measure the hydrodynamic diameter (d_z), polydispersity index (PDI), and zeta potential (ζ) of AgNPs in each NaCl and $MgCl_2$ solution. The instrument was equipped with a 4 mW He-Ne laser (663 nm) and was utilized in backscatter mode at an angle of 173°. All measurements were recorded at 25°C following a 2 min temperature equilibration period. All salt solutions were twice filtered with a 0.20 μm nylon syringe filter. Disposable polystyrene cuvettes were used for analysis and rinsed with the filtered salt solution prior to preparation of the AgNP sample. Working in the dark, BioPure AgNP suspensions were prepared in the filtered salt solution to a total silver concentration of 5 mg L^{-1} (≈1.65×10^{10} particles mL^{-1}), unless otherwise noted. The sample was vortexed for 10 s to homogenize and incubated in the dark at room temperature for 10 min prior to analysis. Zeta potential measurements were conducted using a Pd dip cell and by applying the Smoluchowski equation. Five measurements were recorded for each sample, with 11 or 50 sub-runs per measurement for DLS and zeta potential measurements, respectively.

Particle Impact Voltammetry

A CHI630E electrochemical workstation equipped with a potentiostat, PicoAmp Booster, and Faraday cage was used for PIV analysis (CH Instruments, Inc.). The provided CH software (v. 18.05) was used for data collection and instrument control. PIV was carried out using a three-electrode electrochemical cell with an 11 μm carbon fiber UME working electrode, a platinum wire auxiliary electrode, and a Ag/AgCl reference electrode. The UME was polished daily with 0.05 μm alumina powder and weekly with 1.0 μm, 0.3 μm, and 0.05 μm alumina powders (in succession). Between polishing steps, the UME was thoroughly rinsed and subsequently sonicated in Millipore water for 30 s. After polishing the UME, the PIV/UV-vis cuvette was filled with the appropriate volume of buffer (10 mM citrate – 10 mM NaCl, pH 5.0), assembled with the electrodes, and sparged with $N_2(g)$ and stirred for 10 min (final dissolved oxygen

concentration ≈5.0 mg L^{-1}). Then, the UME was conditioned by cycling 100 times between -0.6 V to +0.6 V at a rate of 0.3 V/s. Next, with sparging turned off, the AgNPs were added to a final concentration of 5.0 mg L^{-1} and stirred to homogenize. Stirring was turned off and after a 5 s quiet time, an amperometric *i-t* curve was recorded for 300 s at a potential of +0.3 V and with a 0.1 s sample interval.

Particle Impact Voltammetry Coupled with UV-vis Spectroscopy

PIV was carried out just as described above, but with online UV-vis spectroscopy for simultaneous detection. An Ocean Optics Flame UV-vis spectrophotometer (Ocean Insights, Inc.) was used to record absorbance spectra and kinetic scans. The provided OceanView software (v. 1.5.7) was used for data collection and instrument control. Once the PIV/UV-vis cuvette was assembled, the UME conditioned, and the UV-vis lamp warmed for an adequate amount of time, AgNP aggregation experiments were initiated. First, AgNPs were added to the cuvette to a final concentration of 5.0 mg L^{-1} and stirred to homogenize. The Ocean Optics spectrometer utilizes a CCD detector, so the λ_{max} of the AgNP LSPR band could be rapidly identified. A kinetic absorbance scan was initiated that monitored the absorbance of the λ_{max} with respect to time. Once the kinetic scan showed a stable absorbance signal for the AgNP sample, the appropriate volume of NaCl or $MgCl_2$ stock solution was added to the cell to reach the desired final concentration (between 10 – 100 mM for NaCl and 1 – 5 mM for $MgCl_2$). The solution was briefly stirred to homogenize (≈5 s), an absorbance spectrum was recorded and an amperometric *i-t* experiment was initiated. PIV and UV-vis kinetics experiments were recorded for 300 s from the initiation of data collection, while absorbance spectra were recorded every 60 s within this time frame.

Absorbance spectra were analyzed to identify any changes in the λ_{max} of the AgNP LSPR

band. Specifically, a decrease in the absorbance at the λ_{max} for the monodisperse AgNP suspension and the appearance of a new absorbance band at longer wavelength were taken as qualitative evidence of AgNP aggregation. To quantify the rate of AgNP aggregation, UV-vis kinetic scans were analyzed over the first 15 s according to[27,32–34,51,52]:

$$k_{aggregation} = \frac{1}{oN}\frac{dA}{dt} \quad (1)$$

where $k_{aggregation}$ is the aggregation rate constant, (dA/dt) is the slope of the UV-vis kinetic scan measured at the λ_{max}, N is the initial particle concentration, and o is the optical factor.[52] In accordance with DLVO theory, aggregation rate constants were measured over several different electrolyte concentrations that spanned the RLCA and DLCA regimes. Then, the attachment efficiencies, α, were calculated according to:

$$\alpha = \frac{k_{slow}}{k_{fast}} \quad (2)$$

where k_{slow} and k_{fast} are the aggregation rate constants in the RLCA and DLCA regimes, respectively.

PIV data were analyzed using OriginPro 2019 (v. 9.6.0.172) to quantify temporal changes in the AgNP diameter and in the frequency of AgNP collisions. Briefly, PIV amperometric curves were integrated to relate each current transient to the diameter of the colliding particle. An automatic baseline was applied, and manual adjustments were made as required to appropriately define the baseline. To distinguish current transients from noise, a 20% peak height threshold was applied. The resulting particle diameters were plotted with respect to time to observe changes in particle diameter upon addition of electrolyte to the PIV/UV-vis cuvette. Separately, the collision frequency (the number of AgNP collisions in the 300 s data collection window) was used to determine the CCC, as will be discussed later. Additional experimental details, including detailed cleaning procedures for PIV/UV-vis, operation of OceanView software, and PIV data

processing are provided in the Electronic Supplementary Information.

RESULTS AND DISCUSSION

General Theory of PIV

PIV has been summarized elsewhere in the literature and is described in more detail in the ESI.[38,53] Here, we provided a brief overview of PIV as it relates specifically to the present study. PIV is an electrochemical technique that monitors single ENM redox events, which are referred to as "particle collisions" or "nano-impacts".[38] In the present work, PIV was carried out in direct oxidation mode to take advantage of the redox activity of Ag. Briefly, by holding the UME at an oxidizing potential, individual AgNPs that diffuse to the electrode surface are completely oxidized. The simultaneous oxidation of all Ag atoms in the AgNP causes a large flux of electrons to be transferred at the UME surface, resulting in a change in current, called a "current transient". The magnitude of the current transient can be correlated to the AgNP diameter (ESI Eqns. S3-S5) and the frequency of collisions can be related to the AgNP concentration.

Optimization of PIV

Before establishing the coupled PIV/UV-vis technique, PIV conditions were optimized independently. Since the electrochemical signal can be strongly influenced by the composition and concentration of the supporting electrolyte,[54] as well as the solution pH,[55] a range of salts (NaCl, KCl, $NaNO_3$, or KNO_3) and solution pH (3-7) were evaluated. The optimal conditions for improving the detection sensitivity (reducing background current and increasing the number of observed current transients) was a buffered solution at pH 5.0 with NaCl as the supporting electrolyte (ESI Figure S1).

To better understand the response of the technique to AgNPs of different size, particle

sizes of 10, 20, 40, and 80 nm were analyzed. The signal-to-noise ratio for 10 nm AgNPs was poor (data not shown) and is consistent with other reports that the lower limit for reliable nanoparticle sizing using PIV is around 6-10 nm.[50] As expected, with increasing particle size, the magnitude of the current transients increased (Figure 1). The collision of a larger AgNP at the electrode surface results in the simultaneous oxidation of a greater number of Ag atoms and a proportional increase in the number of electrons transferred. As a result, a larger current transient is observed with increasing particle size. The AgNPs evaluated in Figure 1 were prepared to the same mass concentration, which necessarily corresponds to a different particle concentration. While the application of PIV for the direct determination of AgNP particle number concentration is beyond the scope of this work, the relationship between the frequency of collisions and the particle concentration is evidenced by a decrease in the number of observed transients for 80 nm AgNPs (≈3 pM) relative to 40 nm AgNPs (≈20 pM) relative to 20 nm AgNPs (≈200 pM). Differences in the rate of diffusion of AgNPs with varying diameter can also influence the collision frequency; however, for this particular experiment, the particle concentration had a more significant impact.

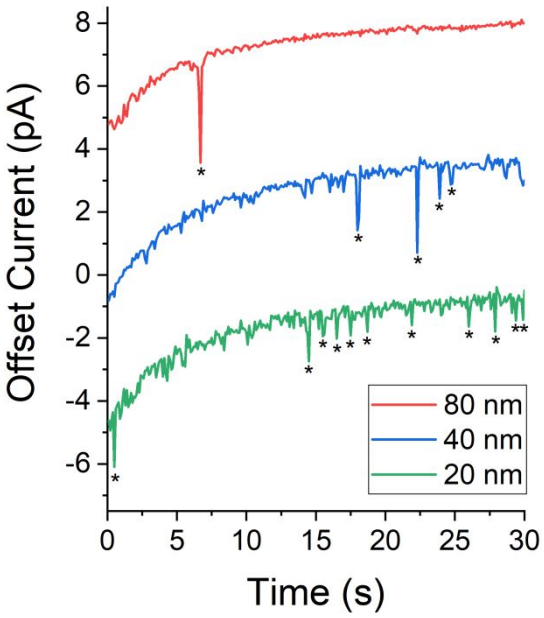

Figure 1. Representative amperometric *i-t* curves demonstrating the effect of AgNP diameter on the magnitude and frequency of current transients observed by PIV. For clarity, current transients are marked with an asterisk (*). NanoXact AgNPs were prepared to a final concentration of 5.0 mg L^{-1} in 10 mM citrate – 10 mM NaCl buffer (pH 5.0).

To confirm that the observed current transients are attributed to faradaic processes, PIV

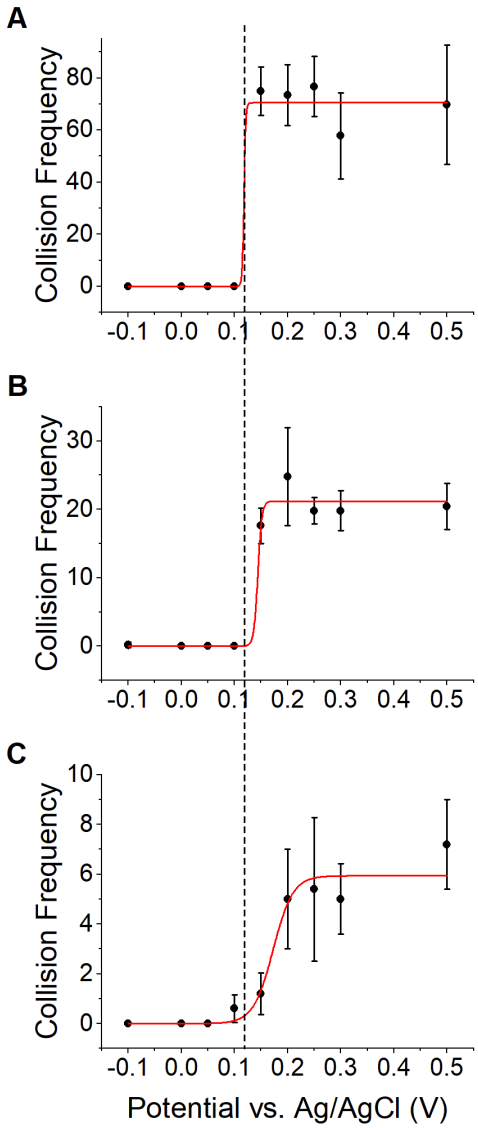

Figure 2. Plots of the AgNP collision frequency (number of collisions per 60 s) as a function of the applied potential for AgNP diameters of **(A)** 20 nm, **(B)** 40 nm, and **(C)** 80 nm. The dashed line indicates the onset potential of current transients for 20 nm AgNPs. A marked anodic shift of the onset potential is observed with increasing AgNP diameter. Error bars represent the standard deviation of 5 independent measurements. NanoXact AgNPs were prepared to a final concentration of 2.0 mg L^{-1} in 10 mM citrate – 10 mM NaCl buffer (pH 5.0).

experiments were carried out over a range of potentials above and below the expected redox potential of Ag(I) (≈0.2 V vs. Ag/AgCl).[56–58] A clear "turn-on" potential was observed at ≈0.12 V for 20 nm AgNPs, ≈0.15 V for 40 nm AgNPs, and ≈0.20 V for 80 nm AgNPs (Figure 2; see Table S1 in the ESI for SEM and DLS characterization of AgNPs). The size-dependent redox

potential of ENMs has been observed by others in the literature and is attributed to a decrease in thermodynamic stability as the particle size decreases.[59–61] For example, in a previous study, zinc oxide nanoparticles were analyzed in acetonitrile at a Hg-modified UME. A positive shift in the half-wave potential (a parameter closely related to the standard potential) of ZnO NPs was observed with decreasing particle diameter as the smaller particles were more easily reduced.[62] In the present study, a decrease in the thermodynamic stability of the 20 nm AgNPs allows it to be more easily oxidized (*i.e.*, at lower, less anodic potentials).

Coupling PIV with UV-vis Spectroscopy

PIV is an emerging technique for the analysis of AgNP aggregation[40,48,49], while UV-vis spectroscopy has been previously used to study colloidal aggregation of AgNPs.[27,32,51] By coupling UV-vis with an orthogonal technique, like PIV, aggregation characteristics can be

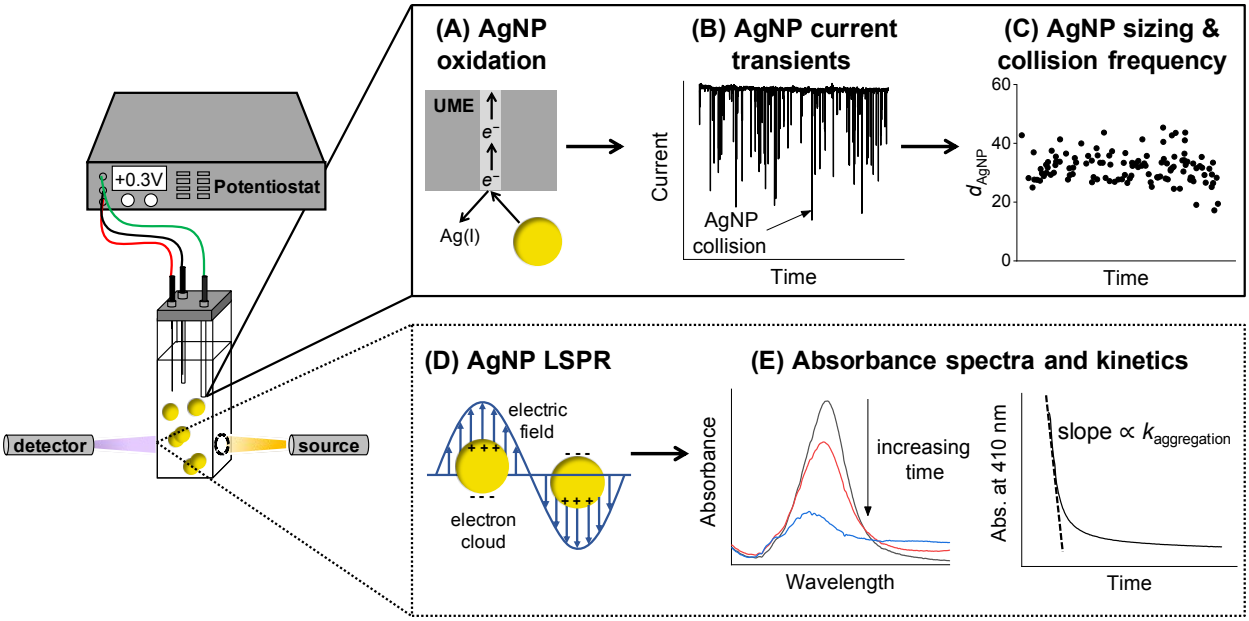

Scheme 1. Diagram of PIV/UV-vis. (A) The working electrode is held at a fixed potential for a specified period of time, during which AgNPs diffuse to the electrode, collide, and are oxidized. **(B)** Each AgNP collision results in a measurable current response (a "current transient"), which is observed in the resulting amperometric *i-t* curve. **(C)** The charge transferred during the collision (area of the current transient peak) is correlated to the number of Ag atoms in the particle and subsequently the diameter of the AgNP. **(D)** Simultaneously, the integrated UV-vis spectrometer is used to probe the AgNP LSPR band and **(E)** measure the decrease in the absorbance signal over time.

quickly and reliably quantified. A schematic of the coupled PIV/UV-vis technique is presented in Scheme 1. Briefly, the workflow for PIV/UV-vis measurements involves the injection of AgNPs into solution, where they diffuse to the UME surface and are oxidized (Scheme 1A). The flux of electrons transferred from each AgNP collision is measured as a current transient in the amperometric *i-t* curve (Scheme 1B). Each transient is integrated offline and correlated to the size of the AgNP that collided with the electrode using Eqns. S1-S3 (see ESI). The diameter of colliding AgNPs (d_{AgNP}) can be plotted over the duration of the experiment to obtain time resolved AgNP sizing and collision frequency data (Scheme 1C). Simultaneously, the LSPR band of AgNPs is monitored using UV-vis spectroscopy (Scheme 1D) by recording an absorbance spectrum every 60 s and measuring the absorbance at 410 nm over time, the slope of which is proportional to the aggregation rate, $k_{aggregation}$ (Scheme 1E).

In order to integrate these two technologies, spectroelectrochemical cuvettes must be employed. However, while spectroelectrochemical cuvettes are commercially available, they are typically designed to support mesh working electrodes, which are not compatible with PIV experiments. Thus, in the present study, a cuvette cap was designed and 3D-printed to support PIV experiments conducted in 1 cm × 1 cm spectroscopy cuvettes (Figures S2-S3; see also the ESI for more information on the design of the PIV/UV-vis cuvette cap and for the 3D printing file). The assembled PIV/UV-vis cuvette accommodated the three-electrode setup for PIV (carbon fiber UME, Ag/AgCl reference electrode, and Pt wire counter electrode), as well as the Teflon sparge line for removing dissolved O_2 from solution, and each of these components was suspended high enough in solution so as not to impede the UV-vis light path (Figure 3; see also Figure S4 in the ESI).

A series of control experiments were performed to assess the functionality of the

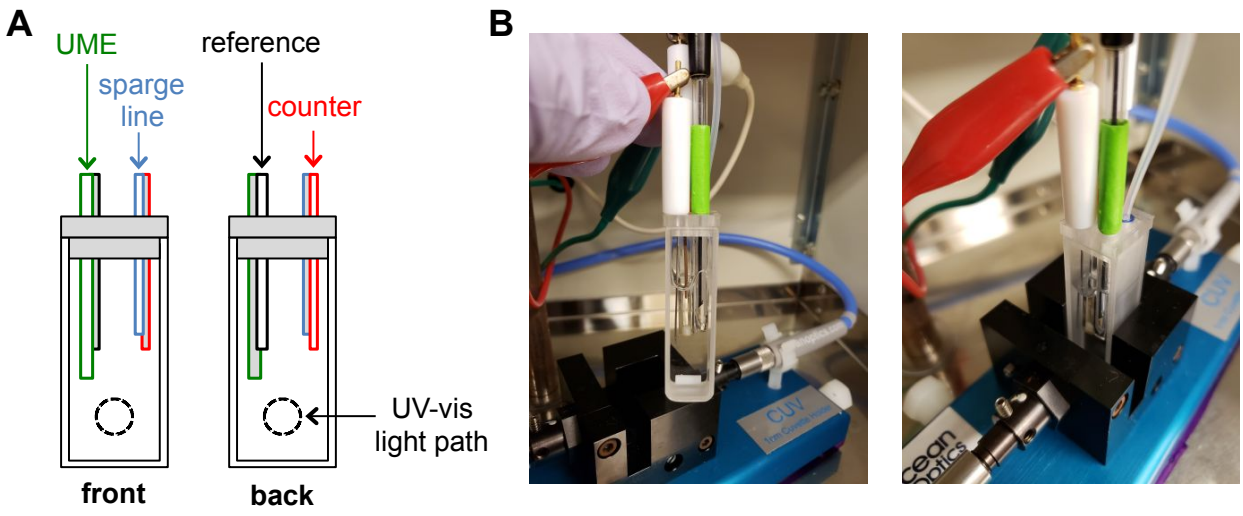

Figure 3. (A) Schematic of the front and back of the PIV/UV-vis cuvette. **(B)** Photographs of the constructed PIV/UV-vis cuvette.

constructed PIV/UV-vis cuvette and the effectiveness of the integrated technologies. First, to determine whether the cell construction had any impact on PIV measurements, five replicate experiments were performed each in either a traditional electrochemical cell or the constructed PIV/UV-vis cuvette. In particular, it was important that the cuvette was air-tight so as to prevent high concentrations of dissolved O_2 from increasing the background current. No significant differences were noted in the amperometric *i-t* curves obtained in a traditional electrochemical cell versus the constructed PIV/UV-vis cuvette (ESI Figure S5).

Next, control experiments were performed to assess whether the integration of these two technologies had any impact on the ability of each individual technique to quantify AgNP aggregation. A sample of 40 nm AgNPs was prepared in a solution containing 40 mM Na^+ so as to induce aggregation. Five replicate experiments were performed each for PIV alone, UV-vis alone, and the combined PIV/UV-vis technique. Qualitatively, the amperometric *i-t* curves obtained by PIV showed no significant differences in the AgNP transient profile or observed signal-to-noise when the experiment was performed alone or with simultaneous UV-vis analysis

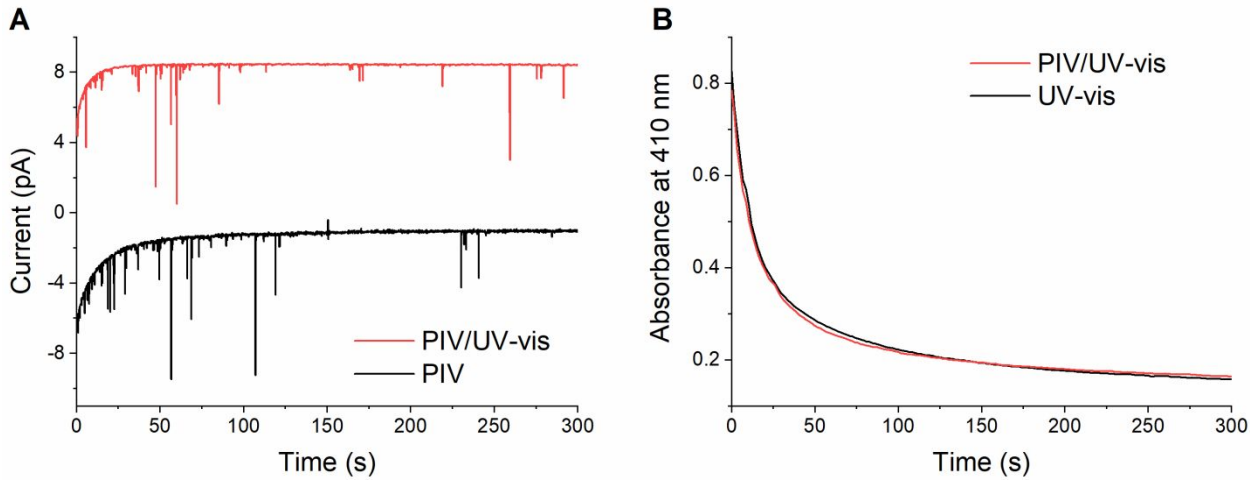

Figure 4. Control experiments demonstrating independent and integrated PIV and UV-vis analyses. **(A)** Representative amperometric *i-t* curves for PIV alone or combined with UV-vis and **(B)** representative kinetic absorbance scans for UV-vis alone or combined with PIV. BioPure 40 nm AgNPs were prepared to a final concentration of 5.0 mg L^{-1} in 10 mM citrate – 40 mM NaCl buffer (pH 5.0).

(Figure 4A). Likewise, UV-vis kinetic experiments showed a remarkably similar decrease in the absorbance at 410 nm as a function of time (Figure 4B). These qualitative observations were supported by a quantitative comparison of AgNP collision frequencies measured by PIV and aggregation rate constants, $k_{aggregation}$, measured by UV-vis. Both aggregation parameters were the same within error whether the methods were performed independently or simultaneously (ESI Table S2). Overall, these control studies provided strong evidence that PIV and UV-vis are truly orthogonal and could be successfully coupled to quantify AgNP aggregation kinetics in real-time.

Using PIV/UV-vis to quantify AgNP aggregation kinetics in the presence of monovalent and divalent cations

As proof-of-principle, the PIV/UV-vis technique was used to measure the CCC of AgNPs in the presence of Na^+ and Mg^{2+} by evaluating a range of concentrations in the RLCA and DLCA regimes. For illustrative purposes, one PIV/UV-vis data set obtained in each regime is presented in Figure 5. At low Na^+ concentration (20 mM; RLCA regime), a significant number of PIV

current transients was observed over the entire 300 s experiment with fairly uniform size (plotted as d_{AgNP} vs. time in Figure 5A). Simultaneously, a marginal decrease in the absorbance measured at 410 nm was observed (Figure 5A). In contrast, at higher Na^+ concentration (80 mM; DLCA regime) a significant decrease in the number of PIV current transients was observed, with no additional transients detected halfway through the 300 s experiment. The increase in Na^+ concentration had no apparent effect on the electrochemical measurement, as evidenced by the stable background current over all concentrations evaluated (ESI Figure S6). Again, the AgNP size determined by PIV was fairly uniform. At the same time, a sharp decrease in the absorbance measured at 410 nm was observed (Figure 5B). These results demonstrate that the disappearance of current transients with increasing Na^+ concentration measured by PIV is analogous to the

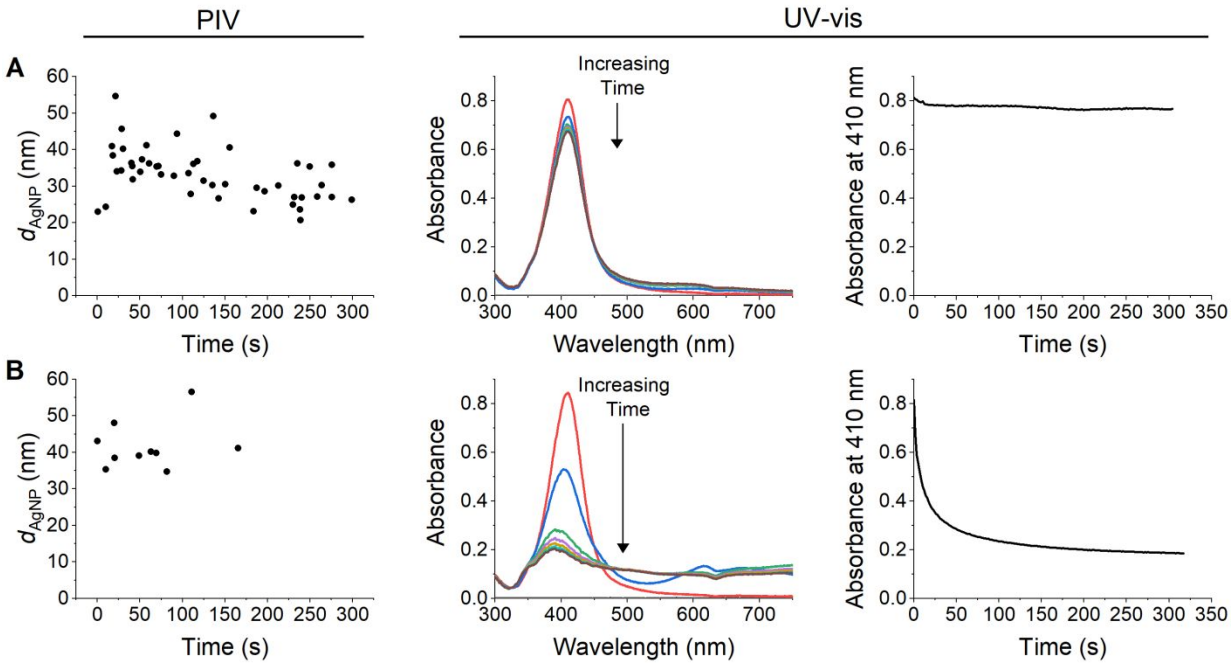

Figure 5. Representative data from the integrated PIV/UV-vis technique. All measurements monitor the behavior of AgNPs over the first 5 min following introduction of **(A)** 20 mM NaCl or **(B)** 80 mM NaCl. Measurements are as follows (from left-to-right): AgNP diameters of individual AgNP collisions determined by PIV, absorption spectra of the AgNP solution recorded every 60 s, and kinetics absorbance scans of the AgNP suspension monitored at 410 nm. BioPure 40 nm AgNPs were prepared to a final concentration of 5.0 mg L^{-1} in 10 mM citrate buffer (pH 5.0) with the indicated concentration of NaCl.

decrease in absorbance of the LSPR band at 410 nm with increasing Na^+ concentration measured by UV-vis (*vide infra*).

As AgNPs aggregate, the λ_{max} of the monodisperse particles dramatically decreases over time and concurrently, the λ_{max} of the aggregated AgNPs shifts to longer wavelength.[27,32,34,63] However, this red shift may not always be observed if the aggregates become so large that they sediment or if the AgNP size distribution becomes too large to produce a defined absorbance peak.[21,31,32,56,63] With increasing Na^+ concentration (from 20 mM to 80 mM), the electric double layer surrounding the AgNPs is compressed to a greater extent leading to faster aggregation rates and a more rapid decrease in the absorbance, which is evidenced in both the absorbance spectra and kinetics scans (Figure 5, UV-vis panel). The rapid decline in absorbance at 410 nm is attributed to a rapid decrease in concentration of monodisperse AgNPs as they begin to aggregate and form larger clusters. At the same time, the small, broad absorbance band observed at approximately 600 nm in the presence of 20 mM Na^+ can be attributed to the LSPR band of the larger AgNP aggregates. While the absorbance intensity of the LSPR band at ≈600 nm is low, the band is distinctly observed only after addition of 20 mM Na^+ when compared to the initial absorbance band of AgNPs (at t = 0 s). Further, the LSPR band at ≈600 nm is not observed in the absorbance spectra of AgNPs under less favorable aggregation conditions (see for comparison the absorbance spectra of AgNPs in 10 mM NaCl in ESI Figure S7). In the presence of 80 mM Na^+, the absorbance band at ≈600 nm further broadened and intensified, which is consistent with the rapid formation of dendritic aggregates in the DLCA regime.[24] AgNP aggregation was confirmed using DLS and shows a significant increase in the hydrodynamic diameter of AgNPs from 50 ± 3 nm in 20 mM Na^+ solutions to 340 ± 20 nm in 80 mM Na^+ solutions (Table 1). Overall, monitoring the rapid decline in absorbance of AgNPs at 410 nm provides a much more

sensitive means for quantifying aggregation, than would monitoring the increase in absorbance at 600 nm.

Table 1. Characterization of AgNPs in NaCl solutions[a]

[NaCl] (mM)	d_{PIV}[b] (nm)	d_{DLS} (nm)	PDI	ζ (mV)
10	41 ± 8	46 ± 2	0.23 ± 0.01	-41 ± 1
20	37 ± 7	50 ± 3	0.43 ± 0.01	-43 ± 1
40	40 ± 10	190 ± 60	0.60 ± 0.01	-48 ± 2
60	39 ± 7	320 ± 20	0.24 ± 0.01	-53 ± 3
80	38 ± 8	340 ± 20	0.24 ± 0.03	-50 ± 2
100	38 ± 7	400 ± 40	0.24 ± 0.02	-54 ± 2

[a]BioPure 40 nm AgNPs were diluted to a concentration of 5.0 mg L^{-1} in 10 mM sodium citrate (pH 5.0) with the indicated concentration of NaCl. For PIV analysis, samples were analyzed immediately after introduction of NaCl. For DLS and zeta potential experiments, samples were incubated for 10 min prior to analysis. All values are reported as the average and standard deviation of 5 replicates.
[b]Diameters of BioPure 40 nm AgNPs were determined by integration of PIV amperometric *i-t* curves and using Eqns. S1-S3 (see ESI)

The measurement of AgNP aggregation kinetics using PIV can also be described as a measurement of the decrease in the concentration of monodisperse AgNPs over time. Recent work has shown that PIV can reliably measure particles between ≈6-100 nm.[50] The large aggregates observed in this work (> 300 nm in the DLCA regime) are simply too large to diffuse to the electrode surface during the time scale of the experiment. This is not to say that large aggregates cannot be measured using PIV, but rather that the slower rates of diffusion of large particles prevent a sufficient number of transients from being measured to provide reliable statistics. Thus, the current transients observed in the experiments presented here were attributed solely to monodisperse AgNPs and a decrease in the frequency of AgNP current transients was

correlated to a decrease in the concentration of monodisperse particles, just as in UV-vis. Further evaluation of the AgNP diameters calculated from PIV amperometric *i-t* curves strengthens the argument that predominately monodisperse AgNPs are generating the observed transients. As measured by PIV, the average AgNP diameter was 37 ± 7 nm in 20 mM Na^+ solutions and 38 ± 8 nm in 80 mM Na^+ solutions (Table 1).

The PIV/UV-vis experiment was performed at a range of Na^+ concentrations (10-100 mM) with five replicates performed at each concentration. To quantify AgNP collision frequencies, PIV amperometric *i-t* curves were integrated and the number of current transients observed during the duration of the experiment (300 s) was tabulated. Collision frequencies (number of AgNP collisions/s) were averaged at each concentration of NaCl and were normalized to the collision frequency in the DLCA regime (collisions/s_{fast}) according to:

$$normalized\ collision\ frequency = \frac{collisions/s}{collisions/s_{fast}} \quad (3)$$

The normalized collision frequencies determined by PIV and the attachment efficiencies determined by UV-vis were plotted as function of the NaCl concentration (Figure 6, see also ESI Table S3). Both plots show a clear transition from the RLCA to the DLCA regime (intersection of the two linear portions of each plot).

For the normalized collision frequency data obtained with PIV, the number of observed transients decreases with increasing Na^+ concentration until approximately 40 mM (Figure 6A). This decrease in observed transients is consistent with an increase in the number of aggregated AgNPs in solution that are too large to diffuse to the electrode. This observation is also consistent with the expected behavior of AgNPs in the RLCA regime, whereby colloidal aggregation is dependent on the electrolyte concentration, with increasing concentration leading to more rapid aggregation. Beyond 40 mM Na^+, the number of observed transients was relatively

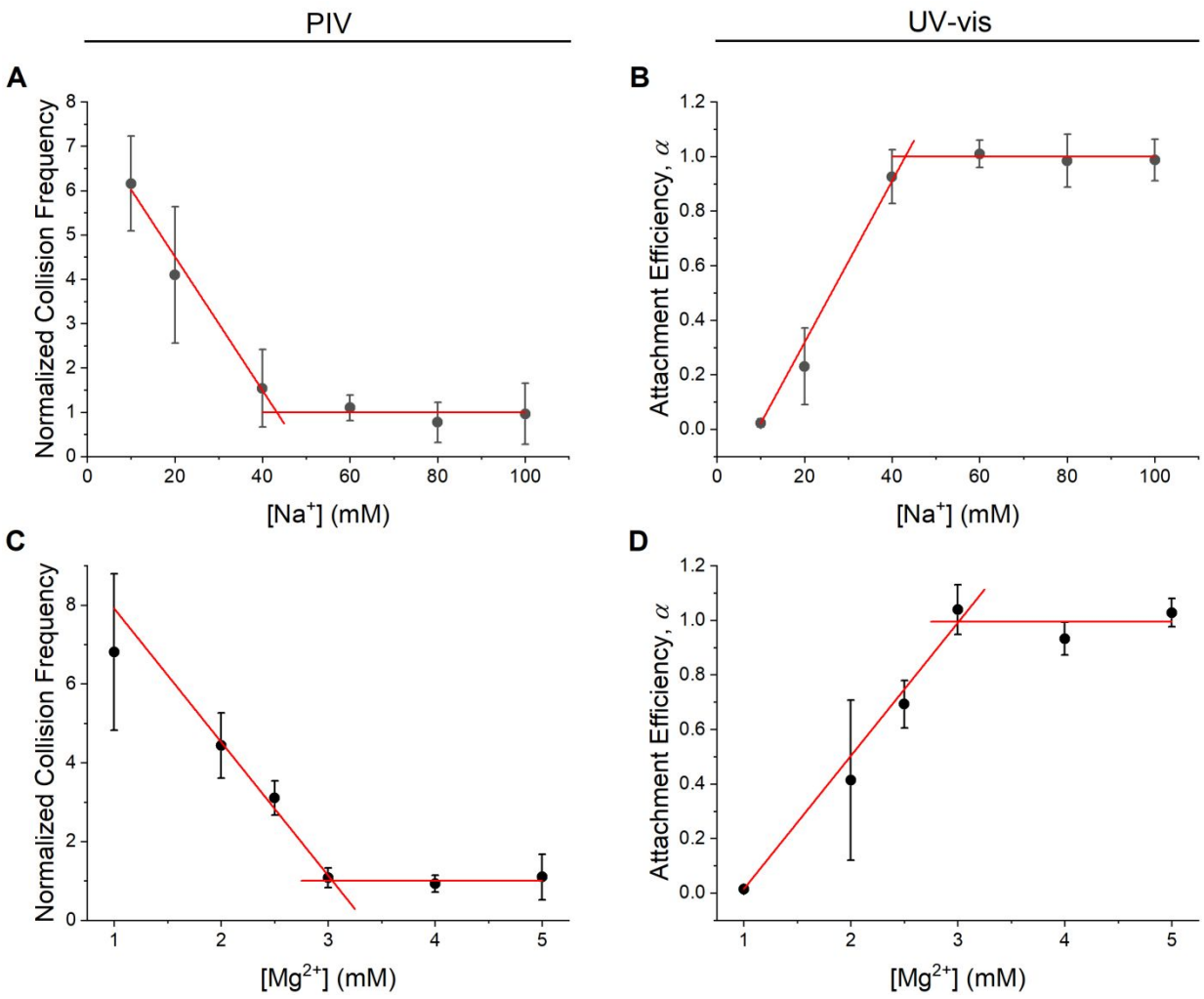

Figure 6. Normalized collision frequency profile determined by PIV **(left)** and attachment efficiency, α, profile determined by UV-vis **(right)** obtained for 40 nm AgNPs in the presence of **(A, B)** a monovalent cation (Na^+) and **(C, D)** a divalent cation (Mg^{2+}). Attachment efficiencies were calculated using Eqns. 1 and 2. The linear fits are extrapolated from the reaction-limited and diffusion-limited regimes (RLCA and DLCA, respectively) and their intersection enables determination of the critical coagulation concentration (CCC). Error bars represent the standard deviation of 5 independent PIV/UV-vis measurements. BioPure 40 nm AgNPs were prepared to a final concentration of 5.0 mg L^{-1} in 10 mM citrate buffer (pH 5.0) with the indicated concentration of the cation.

constant (and relatively infrequent), regardless of further increases in Na^+ concentration (Figure 6A). This is indicative of the DLCA regime, whereby colloidal aggregation is only limited by diffusion; the Na^+ concentration no longer influences the rate of aggregation. Comparing all Na^+ concentrations evaluated, the average AgNP diameter determined by PIV was the same within

error, again indicating that the observed current transients are due to monodisperse AgNPs in solution. UV-vis attachment efficiencies, α (Eqns. 1-2), were also plotted as a function of Na^+ concentration and similar trends were observed, whereby at Na^+ concentrations below 40 mM, AgNP aggregation is concentration-dependent, but at higher concentrations AgNP aggregation is independent of electrolyte concentration (Figure 6B).

These data were also supported by DLS and zeta potential measurements of the AgNPs in each of the solutions. In the RLCA regime, the hydrodynamic diameter of AgNPs increased with increasing Na^+ concentration and PDI values indicated significant sample heterogeneity, whereas in the DLCA regime both measurements indicated a more homogenous solution of highly aggregated AgNPs (Table 1). With increasing Na^+ concentration, the zeta potential of AgNPs increased (became more negative) from around -41 mV at the lowest concentration analyzed to around -53 mV at the CCC. At Na^+ concentrations beyond the CCC, the zeta potential stabilized. In previous studies, the zeta potential of citrate-stabilized AgNPs has been shown to shift to a more positive or a more negative value with increasing electrolyte concentration with the former attributed to increased charge screening by cations[20,27] and the latter to the formation of AgCl NPs or AgCl coatings on the AgNPs.[25,26] Given the shift toward more negative zeta potential observed in this study, it is possible that AgCl NPs or AgCl surface coatings formed at higher Cl^- concentrations, specifically those above the CCC. Further support for this explanation includes the slight blue shift in the absorbance band at 410 nm and a subtle increase in absorbance at 350 nm (Figure 5B), which could be attributed to Rayleigh scattering from AgCl NPs.[64,65] These changes in the absorbance spectra are more pronounced above the CCC, consistent with zeta potential results. For example, in the presence of 10 or 20 mM NaCl (below the CCC) no shift in the absorbance band at 410 nm is observed over time (ESI Figure S7 and Figure 5A,

respectively), but in the presence of 80 mM NaCl (above the CCC), a clear blue shift is observed (Figure 5B).

In accordance with DLVO theory, the CCC was determined as the point of intersection of the RLCA and DLCA regimes. The CCC values extrapolated from the PIV and UV-vis data were remarkably similar, with a Na^+ concentration of 43 ± 4 mM determined using PIV and 43 ± 3 mM using UV-vis (Table 2). Given the exceptional accuracy and precision of these measurements, the PIV/UV-vis technique was also validated with a divalent cation, Mg^{2+}. Divalent cations lead to greater suppression of the electric double layer around the AgNP, so smaller concentrations would lead to more rapid aggregation. Accordingly, the range of Mg^{2+} concentrations analyzed was much smaller (1-5 mM), otherwise the experiment was carried out in the same manner as before. Again, PIV current transients largely represented the concentration of monodisperse AgNPs, as supported by the diameters determined from amperometric *i-t* curves

Table 2. Critical coagulation concentrations (CCC) of AgNPs in the presence of monovalent and divalent cations determined by PIV and UV-vis[a]

Cation	CCC (mM)[b]	
	PIV	UV-vis
Na^+	43 ± 4	43 ± 3
Mg^{2+}	3.0 ± 0.3	3.0 ± 0.1

[a]BioPure 40 nm AgNPs were diluted to a concentration of 5.0 mg L^{-1} in 10 mM sodium citrate buffer at pH 5.0. The cation concentration was varied as reported in Figure 6.
[b]CCCs were determined as the cation concentration at the intersection of the DLCA and RLCA regimes in Figure 6

(ESI Table S4). With increasing concentrations of Mg^{2+} up to ≈3 mM the AgNP collision frequency was concentration-dependent, beyond which the collision frequency was relatively

constant and infrequent (Figure 6C). UV-vis kinetic analysis exhibited similar trends with an increase in the attachment efficiency with increasing Mg^{2+} concentration up to ≈3 mM, beyond which the aggregation rate was constant (Figure 6D). Qualitative analysis of absorbance spectra provided additional evidence of AgNP aggregation behaviors. For example, in the presence of 1.0 mM Mg^{2+}, the absorbance at 410 nm decreased only slightly, suggesting very little AgNP aggregation (ESI Figure S8A). However, in the presence of 3.0 mM Mg^{2+}, the absorbance at 410 nm decreased rapidly and a small, broad peak was observed at ≈550 nm, consistent with the formation of AgNP aggregates (ESI Figure S8B). In all cases, the position of the band at 410 nm was stable and did not undergo a shift in wavelength.

The CCC values obtained for Mg^{2+} by PIV and UV-vis were also in excellent agreement with one another (Table 2) and were strongly supported by DLS and zeta potential analyses (ESI Table S5). Briefly, with increasing Mg^{2+} concentration up to the CCC the hydrodynamic diameter of AgNPs increased and the PDI values were large indicating a heterogenous size distribution. Beyond the CCC, a more homogenous solution of aggregated AgNPs was observed. The zeta potential of AgNPs became more positive with increasing Mg^{2+} concentration, indicative of increased charge screening by Mg^{2+}. Since much lower Cl^- concentrations were employed in this experiment (maximum Cl^- concentration of 10 mM compared to 100 mM for NaCl), there was no evidence either in the zeta potential data or UV-vis spectra to support the formation of AgCl NPs or AgCl surface coatings.

Not only were the CCC values determined by PIV and UV-vis in strong agreement with one another, but they are also well supported by CCC values reported in the literature for citrate stabilized AgNPs (ESI Table S6).[20,25–30] While these studies do not provide an ideal point of comparison due to differences in particle diameters, solution conditions, and the use of different

analysis methods, the CCC values are within a fairly narrow range (around 40-80 mM for Na^+ and 2-3 mM for Mg^{2+}). For instance, the CCC was 70 mM for 58 nm AgNPs[28] and 59 mM for 46 nm AgNPs[30] under similar conditions to those studied here. These values are both slightly higher than the ones obtained in this work. However, in both of these studies, DLS was used to measure the aggregation kinetics, which has been previously shown to yield higher CCC values than UV-vis (ESI Table S6).[27] This is attributed to a difference in the analysis methods, where DLS aggregation experiments measure an increase in the hydrodynamic diameter of AgNPs as a function of time, and as discussed previously, UV-vis measures a decrease in the concentration of monodisperse AgNPs as function of time.[20,25–30] This may also explain the strong agreement between CCC values obtained by PIV and UV-vis, where although they measure different properties of the AgNPs, they both monitor the concentration of monodisperse AgNPs over time and correlate this decrease in concentration to AgNP aggregation.

Outlook

Overall, PIV/UV-vis is an attractive orthogonal technique for the characterization of ENMs due its affordability, rapid data acquisition, and ability to simultaneously provide qualitative analysis of colloidal suspensions (absorbance spectra), quantitative analysis of AgNP aggregation (absorbance kinetics and PIV), and AgNP sizing (PIV). As briefly mentioned in the introduction and described in the ESI, PIV has already begun to be expanded for the analysis of other ENM types and even for the detection of single viruses via ENM-virus tagging.[40–45]

A potential disadvantage of PIV is the requirement of a supporting electrolyte at a sufficiently high concentration, although most relevant biological and environmental media will include salts. Further, recent work has demonstrated that the analysis of Ag using stripping voltammetry can be carried out in the absence of supporting electrolyte, but additional

experimentation is needed to determine if PIV can be carried out in a similar manner.[54] The composition of different supporting electrolytes can also influence the background signal in PIV. Indeed, during optimization of PIV in the present work, we achieved the most favorable PIV signal in solutions containing NaCl compared to KCl, $NaNO_3$, and KNO_3. PIV measurements were still possible with these other supporting electrolytes, however, data processing suffered slightly due to increased background current. Data regarding the sensitivity of PIV for determining particle number concentration are limited, but preliminary work in our lab under similar experimental conditions to those reported here suggests the limit of detection for AgNPs is approximately 0.5 mg L^{-1} using PIV. With further improvements in electrochemical hardware and UME fabrication, greater sensitivity can be achieved. These improvements would also enable the reliable sizing of ENMs below 10 nm, which would expand the lower range of particle sizes that can be evaluated with this technique.

Finally, future work is needed that explores the utility of PIV and/or PIV/UV-vis in realistic environmental and biological solution conditions. One study has shown that PIV can be used to measured AgNPs in optically opaque solutions that would be otherwise difficult to measure using spectroscopic and light scattering techniques.[39] Very preliminary work in our own lab shows that PIV can be used to measure AgNPs in solutions containing humic acid. While the collision frequency is slightly reduced in the humic acid solution relative to a buffer control (from 210 ± 40 collisions/300 s to 180 ± 40 collisions/300 s), sufficient signal is still obtained for reliable AgNP sizing (ESI Figure S9). Beyond evaluating the application of PIV for the analysis of ENMs in relevant environmental conditions, future work should also explore the influence of biomolecules, like proteins, on PIV signals. While biomolecules can interfere with electrochemical measurements, at suitable protein concentrations, AgNPs have been evaluated

without interference from electrode biofouling.[57] Again, the combined PIV/UV-vis technique could be useful to establish a relationship between the PIV signal and ENM protein adsorption (at least for plasmonic ENMs) since the LSPR band is sensitive to changes in the ENM surface.[57] New mathematical models could be used to study protein binding using PIV, as the electron transfer of AgNPs is likely to be altered by the formation of the biocorona. Simultaneous UV-vis measurements could serve as an integrated control toward this end.

CONCLUSION

Here we demonstrated the development and validation of PIV/UV-vis as a novel orthogonal technique for measuring AgNP aggregation in real-time and have provided a simple means to determine CCC values from PIV data. The strength in this technique lies in its ability to simultaneously monitor changes in the redox properties of individual AgNPs and in the spectroscopic properties of the bulk colloidal solution. Using PIV, AgNP collision frequencies (a measure of the concentration of monodisperse AgNPs) and AgNP diameters were quantified, and using UV-vis, aggregation rate constants were quantified. Each of these data sets was used to determine CCC values for AgNPs in the presence of monovalent and divalent cations and results were in strong agreement with one another (≈43 mM Na^+ and ≈3 mM Mg^{2+} as determined by both PIV and UV-Vis). The development of fast, affordable, and reproducible analytical methods is important for the continued evaluation of ENM fate and transport in environmental systems. For these reasons, we believe PIV/UV-vis could be of broad use to the nanotechnology community. Specifically, experimental analysis times are on the order of minutes, the entire PIV/UV-vis experimental set-up can be constructed with commercially available instruments for less than USD 20,000 (or approximately USD 12,000 for PIV alone) and we have shown the

technique to be highly reproducible. The full potential of PIV/UV-vis can be realized by its future application to evaluate ENM aggregation in more complex solution chemistries, to study other physical transformations of ENMs, and for the analysis of other redox active metal and metal oxide nanomaterials (e.g., Au, Cu, ZnO) of commercial importance.

Acknowledgements

This work was carried out in part at the Singh Center for Nanotechnology, part of the National Nanotechnology Coordinated Infrastructure Program, which is supported by the National Science Foundation grant NNCI-1542153.

References

1 *Nanotechnology Update: Corporations Up Their Spending as Revenues for Nano-enabled Products Increase*, Lux Research, Inc., Boston, MA, 2014.

2 L. Pourzahedi, M. Vance and M. J. Eckelman, Life Cycle Assessment and Release Studies for 15 Nanosilver-Enabled Consumer Products: Investigating Hotspots and Patterns of Contribution, *Environ. Sci. Technol.*, 2017, **51**, 7148–7158.

3 M. E. Vance, T. Kuiken, E. P. Vejerano, S. P. McGinnis, M. F. Hochella, D. Rejeski and M. S. Hull, Nanotechnology in the real world: Redeveloping the nanomaterial consumer products inventory, *Beilstein Journal of Nanotechnology*, 2015, **6**, 1769–1780.

4 *Silver Nanoparticles Market by Application (Electronics & Electrical, Healthcare, Food & Beverages, Textiles) and Segment Forecasts to 2022*, Grand View Research, Inc., San Francisco, CA, 2015.

5 B. Le Ouay and F. Stellacci, Antibacterial activity of silver nanoparticles: A surface science insight, *Nano Today*, 2015, **10**, 339–354.

6 M. Murphy, K. Ting, X. Zhang, C. Soo and Z. Zheng, Current Development of Silver Nanoparticle Preparation, Investigation, and Application in the Field of Medicine, *Journal of Nanomaterials*, 2015, **2015**, 1–12.

7 S. Prabhu and E. K. Poulose, Silver nanoparticles: mechanism of antimicrobial action, synthesis, medical applications, and toxicity effects, *Int Nano Lett*, 2012, **2**, 32.

8 M. Konop, T. Damps, A. Misicka and L. Rudnicka, Certain Aspects of Silver and Silver Nanoparticles in Wound Care: A Minireview, *Journal of Nanomaterials*, 2016, **2016**, 1–10.

9 E. M. Sussman, P. Jayanti, B. J. Dair and B. J. Casey, Assessment of total silver and silver nanoparticle extraction from medical devices, *Food and Chemical Toxicology*, 2015, **85**, 10–19.

10 T. M. Benn and P. Westerhoff, Nanoparticle Silver Released into Water from Commercially Available Sock Fabrics, *Environ. Sci. Technol.*, 2008, **42**, 4133–4139.

11 J. Hedberg, S. Skoglund, M.-E. Karlsson, S. Wold, I. Odnevall Wallinder and Y. Hedberg, Sequential Studies of Silver Released from Silver Nanoparticles in Aqueous Media Simulating Sweat, Laundry Detergent Solutions and Surface Water, *Environ. Sci. Technol.*, 2014, **48**, 7314–7322.

12 K. Kulthong, S. Srisung, K. Boonpavanitchakul, W. Kangwansupamonkon and R. Maniratanachote, Determination of silver nanoparticle release from antibacterial fabrics into artificial sweat, *Particle and Fibre Toxicology*, 2010, **7**, 8.

13 P. V. AshaRani, G. Low Kah Mun, M. P. Hande and S. Valiyaveettil, Cytotoxicity and Genotoxicity of Silver Nanoparticles in Human Cells, *ACS Nano*, 2009, **3**, 279–290.

14 N. Durán, C. P. Silveira, M. Durán and D. S. T. Martinez, Silver nanoparticle protein corona and toxicity: a mini-review, *Journal of Nanobiotechnology*, 2015, **13**, 1–17.

15 S. León-Silva, F. Fernández-Luqueño and F. López-Valdez, Silver Nanoparticles (AgNP) in the Environment: a Review of Potential Risks on Human and Environmental Health, *Water, Air, & Soil Pollution*, 2016, **227**, 1–20.

16 S. M. Louie, R. Ma and G. V. Lowry, in *Frontiers of Nanoscience*, Elsevier, 2014, vol. 7, pp. 55–87.

17 E. Navarro, A. Baun, R. Behra, N. B. Hartmann, J. Filser, A.-J. Miao, A. Quigg, P. H. Santschi and L. Sigg, Environmental behavior and ecotoxicity of engineered nanoparticles to algae, plants, and fungi, *Ecotoxicology*, 2008, **17**, 372–386.
18 Y. Su, V. E. T. M. Ashworth, N. K. Geitner, M. R. Wiesner, N. Ginnan, P. Rolshausen, C. Roper and D. Jassby, Delivery, Fate, and Mobility of Silver Nanoparticles in Citrus Trees, *ACS Nano*, 2020, **14**, 2966–2981.
19 I. Fernando and Y. Zhou, Impact of pH on the stability, dissolution and aggregation kinetics of silver nanoparticles, *Chemosphere*, 2019, **216**, 297–305.
20 K. A. Huynh and K. L. Chen, Aggregation Kinetics of Citrate and Polyvinylpyrrolidone Coated Silver Nanoparticles in Monovalent and Divalent Electrolyte Solutions, *Environmental Science & Technology*, 2011, **45**, 5564–5571.
21 P. Lodeiro, E. P. Achterberg, C. Rey-Castro and M. S. El-Shahawi, Effect of polymer coating composition on the aggregation rates of Ag nanoparticles in NaCl solutions and seawaters, *Science of The Total Environment*, 2018, **631–632**, 1153–1162.
22 M. K. Alqadi, O. A. Abo Noqtah, F. Y. Alzoubi, J. Alzouby and K. Aljarrah, pH effect on the aggregation of silver nanoparticles synthesized by chemical reduction, *Mater Sci-Pol*, 2014, **32**, 107–111.
23 A. M. E. Badawy, T. P. Luxton, R. G. Silva, K. G. Scheckel, M. T. Suidan and T. M. Tolaymat, Impact of Environmental Conditions (pH, Ionic Strength, and Electrolyte Type) on the Surface Charge and Aggregation of Silver Nanoparticles Suspensions, *Environ. Sci. Technol.*, 2010, **44**, 1260–1266.
24 W. Zhang, in *Nanomaterial*, eds. D. G. Capco and Y. Chen, Springer Netherlands, Dordrecht, 2014, vol. 811, pp. 19–43.
25 X. Li, J. J. Lenhart and H. W. Walker, Dissolution-Accompanied Aggregation Kinetics of Silver Nanoparticles, *Langmuir*, 2010, **26**, 16690–16698.
26 X. Li, J. J. Lenhart and H. W. Walker, Aggregation Kinetics and Dissolution of Coated Silver Nanoparticles, *Langmuir*, 2012, **28**, 1095–1104.
27 M. Baalousha, Y. Nur, I. Römer, M. Tejamaya and J. R. Lead, Effect of monovalent and divalent cations, anions and fulvic acid on aggregation of citrate-coated silver nanoparticles, *Science of The Total Environment*, 2013, **454–455**, 119–131.
28 A. M. El Badawy, K. G. Scheckel, M. Suidan and T. Tolaymat, The impact of stabilization mechanism on the aggregation kinetics of silver nanoparticles, *Science of The Total Environment*, 2012, **429**, 325–331.
29 S.-F. Chen and H. Zhang, Stability and sedimentation of silver nanoparticles in the presence of monovalent, divalent and trivalent electrolyte solutions, *Water Science and Technology*, 2014, **70**, 361–366.
30 D. Lin, S. Ma, K. Zhou, F. Wu and K. Yang, The effect of water chemistry on homoaggregations of various nanoparticles: Specific role of Cl − ions, *Journal of Colloid and Interface Science*, 2015, **450**, 272–278.
31 M. E. Osman, M. M. Eid, O. kolthoum H. Khattab, S. M. El-Hallouty, S. M. El-Marakby and D. A. Mahmoud, Spectroscopic characterization of the effect of gamma radiation on the physical parameters of biosynthesized silver/chitosan nano-particles and their antimicrobial activity, *Materials Research Express*, 2015, **2**, 095023.
32 K. Afshinnia and M. Baalousha, Effect of phosphate buffer on aggregation kinetics of citrate-coated silver nanoparticles induced by monovalent and divalent electrolytes, *Science of The Total Environment*, 2017, **581–582**, 268–276.

33 P. Lodeiro, E. P. Achterberg, J. Pampín, A. Affatati and M. S. El-Shahawi, Silver nanoparticles coated with natural polysaccharides as models to study AgNP aggregation kinetics using UV-Visible spectrophotometry upon discharge in complex environments, *Science of The Total Environment*, 2016, **539**, 7–16.

34 K. Afshinnia, I. Gibson, R. Merrifield and M. Baalousha, The concentration-dependent aggregation of Ag NPs induced by cystine, *Science of The Total Environment*, 2016, **557–558**, 395–403.

35 X. Xiao and A. J. Bard, Observing Single Nanoparticle Collisions at an Ultramicroelectrode by Electrocatalytic Amplification, *J. Am. Chem. Soc.*, 2007, **129**, 9610–9612.

36 X. Xiao, F.-R. F. Fan, J. Zhou and A. J. Bard, Current Transients in Single Nanoparticle Collision Events, *Journal of the American Chemical Society*, 2008, **130**, 16669–16677.

37 A. Boika and A. J. Bard, Time of First Arrival in Electrochemical Collision Experiments as a Measure of Ultralow Concentrations of Analytes in Solution, *Analytical Chemistry*, 2015, **87**, 4341–4346.

38 W. Cheng and R. G. Compton, Electrochemical detection of nanoparticles by 'nano-impact' methods, *TrAC Trends in Analytical Chemistry*, 2014, **58**, 79–89.

39 H. S. Toh and R. G. Compton, 'Nano-impacts': An Electrochemical Technique for Nanoparticle Sizing in Optically Opaque Solutions, *ChemistryOpen*, 2015, **4**, 261–263.

40 Y.-G. Zhou, N. V. Rees and R. G. Compton, The Electrochemical Detection and Characterization of Silver Nanoparticles in Aqueous Solution, *Angewandte Chemie International Edition*, 2011, **50**, 4219–4221.

41 Y.-G. Zhou, N. V. Rees, J. Pillay, R. Tshikhudo, S. Vilakazi and R. G. Compton, Gold nanoparticles show electroactivity: counting and sorting nanoparticles upon impact with electrodes, *Chem. Commun.*, 2012, **48**, 224–226.

42 A. R. Jung, S. Lee, J. W. Joo, C. Shin, H. Bae, S. G. Moon and S. J. Kwon, Potential-Controlled Current Responses from Staircase to Blip in Single Pt Nanoparticle Collisions on a Ni Ultramicroelectrode, *Journal of the American Chemical Society*, 2015, **137**, 1762–1765.

43 S. J. Kwon, F.-R. F. Fan and A. J. Bard, Observing Iridium Oxide (IrO_x) Single Nanoparticle Collisions at Ultramicroelectrodes, *Journal of the American Chemical Society*, 2010, **132**, 13165–13167.

44 N. Perera, N. Karunathilake, P. Chhetri and M. A. Alpuche-Aviles, Electrochemical Detection and Sizing of Colloidal ZnO Nanoparticles, *Analytical Chemistry*, 2015, **87**, 777–784.

45 L. Sepunaru, B. J. Plowman, S. V. Sokolov, N. P. Young and R. G. Compton, Rapid electrochemical detection of single influenza viruses tagged with silver nanoparticles, *Chemical Science*, 2016, **7**, 3892–3899.

46 S. J. Kwon and A. J. Bard, DNA Analysis by Application of Pt Nanoparticle Electrochemical Amplification with Single Label Response, *Journal of the American Chemical Society*, 2012, **134**, 10777–10779.

47 J. E. Dick, C. Renault and A. J. Bard, Observation of Single-Protein and DNA Macromolecule Collisions on Ultramicroelectrodes, *Journal of the American Chemical Society*, 2015, **137**, 8376–8379.

48 N. V. Rees, Y.-G. Zhou and R. G. Compton, The Aggregation of Silver Nanoparticles in Aqueous Solution Investigated via Anodic Particle Coulometry, *ChemPhysChem*, 2011, **12**, 1645–1647.
49 J. Ellison, K. Tschulik, E. J. E. Stuart, K. Jurkschat, D. Omanović, M. Uhlemann, A. Crossley and R. G. Compton, Get More Out of Your Data: A New Approach to Agglomeration and Aggregation Studies Using Nanoparticle Impact Experiments, *ChemistryOpen*, 2013, **2**, 69–75.
50 T. R. Bartlett, S. V. Sokolov and R. G. Compton, Electrochemical Nanoparticle Sizing Via Nano-Impacts: How Large a Nanoparticle Can be Measured?, *ChemistryOpen*, 2015, **4**, 600–605.
51 X. Li and J. J. Lenhart, Aggregation and Dissolution of Silver Nanoparticles in Natural Surface Water, *Environmental Science & Technology*, 2012, **46**, 5378–5386.
52 J. W. Virden and J. C. Berg, The use of photon correlation spectroscopy for estimating the rate constant for doublet formation in an aggregating colloidal dispersion, *Journal of colloid and interface science*, 1992, **149**, 528–535.
53 N. V. Rees, Y.-G. Zhou and R. G. Compton, Making contact: charge transfer during particle–electrode collisions, *RSC Adv.*, 2012, **2**, 379–384.
54 K. Ngamchuea, C. Batchelor-McAuley and R. G. Compton, Anodic stripping voltammetry of silver in the absence of electrolytes: Theory and experiment, *Journal of Electroanalytical Chemistry*, 2018, **830–831**, 122–130.
55 P. L. Runnels, J. D. Joseph, M. J. Logman and R. M. Wightman, Effect of pH and Surface Functionalities on the Cyclic Voltammetric Responses of Carbon-Fiber Microelectrodes, *Anal. Chem.*, 1999, **71**, 2782–2789.
56 J. Hui, Z. J. O'Dell, A. Rao and K. R. Riley, In Situ Quantification of Silver Nanoparticle Dissolution Kinetics in Simulated Sweat Using Linear Sweep Stripping Voltammetry, *Environmental Science & Technology*, 2019, **53**, 13117–13125.
57 D. J. Boehmler, Z. J. O'Dell, C. Chung and K. R. Riley, Bovine Serum Albumin Enhances Silver Nanoparticle Dissolution Kinetics in a Size- and Concentration-Dependent Manner, *Langmuir*, 2020, **36**, 1053–1061.
58 T. Romih, S. B. Hočevar, A. Jemec and D. Drobne, Bismuth film electrode for anodic stripping voltammetric measurement of silver nanoparticle dissolution, *Electrochimica Acta*, 2016, **188**, 393–397.
59 W. J. Plieth, Electrochemical Properties of Small Clusters of Metal Atoms and Their Role in Surface Enhanced Raman Scattering, *J. Chem. Phys.*, 1982, **86**, 3166–3170.
60 A. Henglein, The Reactivity of Silver Atoms in Aqueous Solutions (A γ-Radiolysis Study), *Berichte der Bunsengesellschaft für physikalische Chemie*, 1977, **81**, 556–561.
61 R. Tausch-Treml, A. Henglein and J. Lilie, Reactivity of Silver Atoms in Aqueous Solution II. A Pulse Radiolysis Study, *Berichte der Bunsengesellschaft für physikalische Chemie*, 1978, **82**, 1335–1343.
62 N. Perera, N. Karunathilake, P. Chhetri and M. A. Alpuche-Aviles, Electrochemical Detection and Sizing of Colloidal ZnO Nanoparticles, *Analytical Chemistry*, 2015, **87**, 777–784.
63 M. A. Garcia, Surface plasmons in metallic nanoparticles: fundamentals and applications, *J. Phys. D: Appl. Phys.*, 2012, **45**, 389501.

64 J. M. Zook, S. E. Long, D. Cleveland, C. L. A. Geronimo and R. I. MacCuspie, Measuring silver nanoparticle dissolution in complex biological and environmental matrices using UV–visible absorbance, *Analytical and Bioanalytical Chemistry*, 2011, **401**, 1993–2002.

65 J. M. Zook, R. I. MacCuspie, L. E. Locascio, M. D. Halter and J. T. Elliott, Stable nanoparticle aggregates/agglomerates of different sizes and the effect of their size on hemolytic cytotoxicity, *Nanotoxicology*, 2011, **5**, 517–530.

This work describes the development of a novel, robust, and rapid analytical technique that couples single nanoparticle electrochemistry and UV-vis spectroscopy to determine aggregation kinetics and critical coagulation concentrations (CCCs) of silver nanoparticles.